The X-ray spectra of the flaring and quiescent states of YZ CMi observed by *XMM–Newton*

A. J. J. Raassen,[1,2][*] U. Mitra-Kraev[3,4] and M. Güdel[5]

[1]*SRON Netherlands Institute for Space Research, Sorbonnelaan 2, 3584 CA Utrecht, the Netherlands*
[2]*Astronomical Institute 'Anton Pannekoek', Kruislaan 403, 1098 SJ Amsterdam, the Netherlands*
[3]*Department of Applied Mathematics, University of Sheffield, Hicks Building, Sheffield S3 7RH*
[4]*University College London, Mullard Space Science Laboratory, Holmbury St Mary, Dorking, Surrey RH5 6NT*
[5]*Paul Scherrer Institut, Würenlingen & Villigen, 5232 Villigen PSI, Switzerland*

ABSTRACT

We analyse the X-ray spectrum of the active late-type star YZ CMi (M4.5V); for quiescent as well as active stages, we derive emission measure (EM) distributions, elemental abundances, and electron temperatures and densities, which are in turn used to estimate flare loop lengths as well as coronal magnetic field strengths.

YZ CMi was observed in the wavelength range 1–40 Å by the X-ray detectors RGS, EPIC-MOS and EPIC-pn onboard *XMM–Newton*. Some flares occurred during the observation. We perform a multi-temperature fit and model the differential EM of both the flaring and the quiescent parts of the spectrum and derive the coronal temperature distribution, EMs, and elemental abundances of the flaring and quiescent states.

The observed temperature covers a range from about 1.3 to 42 MK. The total volume EM in this temperature interval is $13.7 \pm .8 \times 10^{50}$ cm^{-3} for the quiescent state and $21.7 \pm 1.4 \times 10^{50}$ cm^{-3} for the active state. The abundance pattern in the quiescent state shows some depletion of low first ionization potential (FIP) elements relative to high-FIP elements, indicating the presence of an I(nverse)FIP effect in this active star. No abundance differences between the quiescent and the active states are established.

Based on the X-ray light curves in combination with the temperature, density and EM, the coronal magnetic field strength at flare-site is found to be between 50 and 100 G and the flaring loop lengths are estimated to be in the range of 5–13×10^9 cm.

Key words: techniques: spectroscopic – stars: coronae – stars: flare – stars: individual: YZ CMi – stars: late-type – X-rays: stars.

1 INTRODUCTION

X-ray emission of late-type stars (spectral classes F–M) reveals many properties reminiscent of the X-ray emission from the solar corona. Modern interpretation of the phenomenology revealed in sensitive X-ray observations of cool stars has therefore been guided by the solar analogy, although caution is in order as coronae of magnetically active stars reach temperatures and luminosities outside obvious flares that are uncommon to the Sun; also, flares on many active stars dwarf their solar counterparts not only in energy, but also in their occurrence rate. Despite these potential differences, there is ample evidence that solar concepts do apply to active stellar coronae even during extreme conditions. For example, the chromospheric evaporation process held responsible for the

plasma filling of coronal magnetic loops during the early stages of solar flares has found considerable support from X-ray spectroscopic and photometric observations of active stars. The increase in electron density by orders of magnitude during the initial flare stage has now been recorded spectroscopically (Güdel et al. 2002, 2004) in analogy to previous reports on solar flares (e.g. Doschek et al. 1981); the preceding optical burst signatures provide further support for the standard (solar) flare model in which accelerated coronal electrons stream into the chromosphere, thus driving evaporation of chromospheric material into the corona as the dense material is explosively heated (Güdel et al. 2004; Mitra-Kraev et al. 2005a).

Active M-dwarfs, characterized by a high occurrence rate of large optical flares (Pettersen 1989), have figured prominently in previous studies of stellar X-ray flares (e.g. Raassen et al. 2003a; Mitra-Kraev et al. 2005a; Smith, Güdel & Audard 2005), given their frequency and their relatively short time-scales that make them

---

[*]E-mail: a.j.j.raassen@sron.nl

Table 1. Observation log of the data of YZ CMi. In the last column the wavelength range used during the fitting procedure is given.

Instrument	Filter	Mode	Date of observation (start)	Date of observation (end)	Duration (s)	Wavelength range
RGS1	None	Spec+Q	2000-10-09T06:33:10	2000-10-09T14:10:10	27 416	8–38 Å
RGS2	None	Spec+Q	2000-10-09T06:33:10	2000-10-09T14:10:12	27 418	8–38 Å
MOS1	Medium	Small window	2000-10-09T06:41:56	2000-10-09T14:00:11	26 295	1–14 Å
MOS2	Medium	Timing	2000-10-09T06:52:19	2000-10-09T14:01:32	25 753	–
pn	Medium	Small window	2000-10-09T06:55:33	2000-10-09T14:08:53	26 000	1–14 Å

convenient for study. As exemplified by the above stellar observations, high-resolution spectroscopy now available from *XMM–Newton* (Brinkman et al. 2001; Jansen et al. 2001) and *Chandra* (Brinkman et al. 2000; Canizares et al. 2000) has considerably contributed to our view of large stellar flares, although new riddles have emerged as well. Perhaps the most prominent among those are element abundance anomalies both in flaring and in non-flaring coronal plasmas that are at variance with solar behaviour. In the latter, elements with a low first ionization potential (FIP) are enriched in certain parts of the corona (e.g. Feldman 1992, signifying the so-called solar FIP effect). Although abundance anomalies were suggested previously from low-resolution X-ray spectroscopy (e.g. White et al. 1994), high-resolution X-ray spectroscopy identified an *inversion* of the solar trend, with low-FIP elements being underabundant with respect to higher-FIP elements (IFIP) (Brinkman et al. 2001). Solar-like distributions have been found as well (Raassen et al. 2003b). These anomalies have been studied systematically by Audard et al. (2003, for active binaries) and Telleschi et al. (2005, for solar analogues), now suggesting that the IFIP effect changes towards a solar-type FIP effect as activity declines. Recently, Laming (2004) gave an explanation for both coronal abundance distributions on the basis of ponderomotive forces.

The situation is less clear for flares. In solar flares, coronal abundances tend to return to near-photospheric abundances (e.g. review by Jordan et al. 1998), and corresponding trends (enhancement of the metallicity) have been recorded for active stars (e.g. Mewe et al. 1997). Some flares revealed a solar-like FIP effect (Güdel et al. 1999; Osten et al. 2000; Audard, Güdel & Mewe 2001) although absence of a fractionation has been suggested in others (Osten et al. 2003; Güdel et al. 2004). It is well possible that the topology of the magnetic fields, perhaps inducing different types of flare processes, plays a role for the plasma composition. Although the magnetic field geometry is not directly measurable, various approaches are available to study their extent and structure (see overview in Güdel 2004). For example, Mitra-Kraev et al. (2005b) determined characteristic lengths of flaring loops for a flare observed in AT Mic, using three different approaches [acoustic waves, radiative cooling, and pressure balance (PB)]. Based on a different strategy, Güdel et al. (2004) and Reale et al. (2004) modelled flaring structures on Proxima Centauri based on hydrodynamic simulations, scalings related to plasma cooling, and magnetic loop-arcade models. Here, we plan to apply some of this methodology to a series of flares that have been observed from the dMe star YZ CMi using high- and low-resolution spectroscopy from *XMM–Newton*. At the same time, we will characterize the flaring plasma in terms of temperature and composition and put our results into context with previous observations.

This paper is structured as follows. Section 2 presents the target, the observations and analysis method. Multi-temperature spectral fits are given in Section 3, while Section 4 deals with individual line flux measurements. Electron densities are derived in Section 5.

Section 6 estimates flare loop lengths and magnetic field strengths. We end with a brief discussion and conclusions in Section 7.

2 OBSERVATIONS

YZ CMi (GJ 285) is a M4.5V dwarf at a distance of 5.93 pc (Perryman et al. 1997). Its surface temperature is 2900 K. The stellar radius is $\sim 0.36 \, R_\odot$ (Mullan et al. 1992) and the stellar mass is $\sim 0.34 \, M_\odot$ (Lim, Vaughan & Nelson 1987).

The spectra of YZ CMi were obtained with all instruments on-board *XMM–Newton* on 2000 October 9 during 27 ks. The log of the observations is shown in Table 1.

The data have been reduced with SAS version 5.4.1. No significant contamination by solar flare protons was found. Using rgsproc, we have extracted the first-order spectra for RGS from a cut of 95 per cent of the cross-dispersion point spread function (xpsfincl = 95), and of 95 per cent of the pulse height (pdistincl = 95). The background spectra were obtained by excluding 98 per cent of the cross-dispersion (xpsfexcl = 98).

In the EPIC data no pile-up was noted. Therefore, the spectra of EPIC data were extracted from a circular area around the source with a radius of 50 arcsec for the pn detector and 40 arcsec for the MOS1 detector. Due to instrumental problems, the MOS2 detector, which was in timing mode, did not produce valuable data. The response matrices and ancillary files were produced using rmfgen and arfgen.

Thanks to the high effective area of EPIC, high-quality light curves could be obtained. The same circular area around the source was used as for the spectral extraction. The light curves of EPIC-pn (top panel) and EPIC-MOS (middle panel) and the EPIC-pn hardness ratio (bottom panel) are shown in Fig. 1. The hardness ratio is defined as the ratio of counts in the range above 1 keV to those in the range below 1 keV. The curves are binned in time bins of 40 s. The light curves are corrected for the background. As the total number of background counts is less than 2 per cent of the number of source counts, the influence of the background is, however, negligible. The curves show clear variability, due to stellar flares and coronal activity. The first 15 ks of the observation is, within the sensitivity limits of this observation, quiescent, while the second part (12 ks) is active. In the second part of the observation, two individual flares can be distinguished. They are indicated in Fig. 1 as flare 1 and flare 2. In between these flares, a period of enhanced activity is noted.

We have split the observations into two parts with time cuts covering the first, quiescent 15 ks (from the start of the observation to the beginning of flare 1) and the remaining active 12 ks (from the beginning of flare 1 until the end of the observation). The latter has also been divided into smaller intervals covering the two individual flares only. For the quiescent state, the active state, and the two individual flares, spectra were extracted for all instruments (except for MOS2). The spectra are corrected for the background. However, the time-intervals of the individual flares (durations of 2.2 and
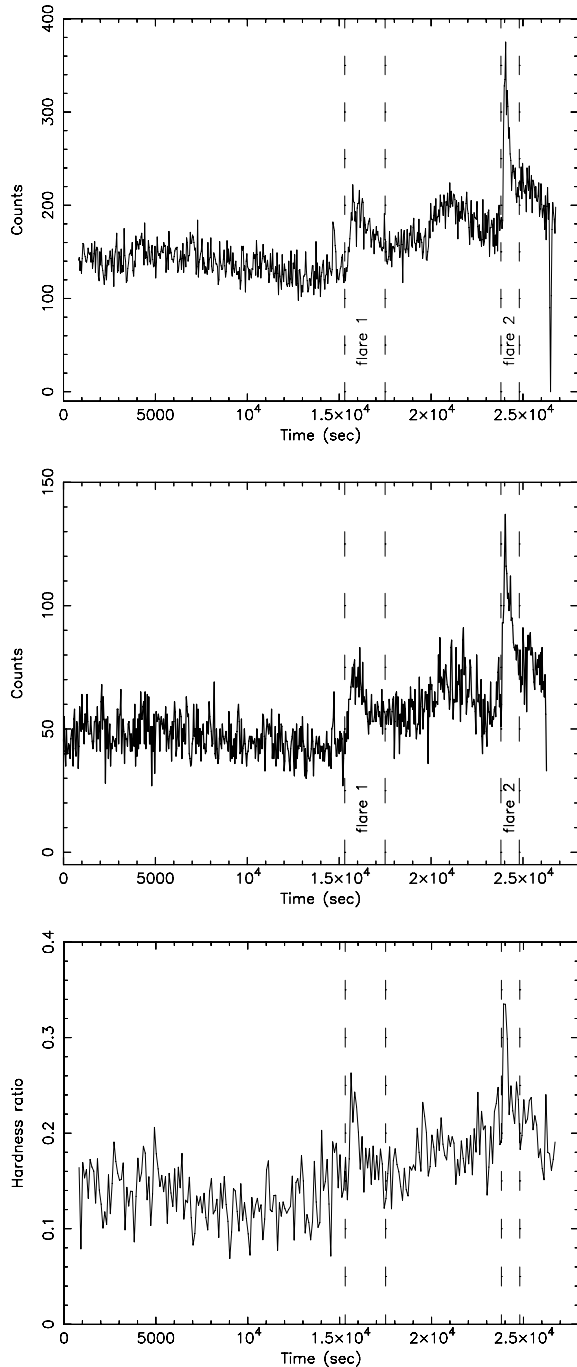
Figure 1. Light curves of YZ CMi, observed with EPIC-pn (top panel) and EPIC-MOS1 (middle panel). The light curves are corrected for the background. The bottom panel shows the hardness ratio based on EPIC-pn. This hardness ratio is the count rate above 1 keV divided by the count rate below 1 keV. The data are re-binned to 40 s, except for the bottom panel. In that panel the time bin is 100 s.

1.0 ks) are short and the spectra therefore have very low signal-to-noise ratios (S/Ns).

3 MULTI-TEMPERATURE FITTING

The interpretation of thermal, coronal spectra has seen some debate since the advent of high-resolution spectroscopy and the consequent

availability of many spectral lines that are excellent discriminators for temperatures and elemental abundances. Various approaches have been developed (see discussion in Güdel 2004), although the basic results appear to be less dependent on the methodology than on the still significant systematic uncertainties in, and the incompleteness of, the atomic physics tabulations. In particular, Audard et al. (2004) and Telleschi et al. (2005) have studied several cases of coronal spectra using approaches that make use of the binned spectra, on the one hand, and of a list of extracted line fluxes on the other. In both cases, satisfactory agreement was obtained for the thermal emission measure (EM) structure and the coronal abundances.

Here, we chose to analyse the EPIC and RGS spectra using multithermal models for optically thin plasma in collisional ionization equilibrium as implemented in SPEX (Kaastra, Mewe & Nieuwenhuijzen 1996a) in combination with MEKAL (Mewe, Kaastra & Liedahl 1995; Kaastra et al. 1996b). The ionization equilibrium is based on calculations by Arnaud & Rothenflug (1985).

3.1 A 10-temperature model for the quiescent and active states

Recently, the EPIC and RGS spectra of YZ CMi were studied based on three isothermal plasma components (Raassen 2005). Here we apply a multi-temperature fit with 10 different thermal components on a grid. This method is somewhat similar to one of the approaches discussed by Telleschi et al. (2005) and Audard et al. (2004). For this case, the temperatures were fixed on a grid between 0.02 and 10.24 keV with a binwidth of 0.3 dex, that is, in steps of a factor of 2.0 in temperature.

The approach of 10 fixed temperatures is preferred over the usual three- or four-temperature fit, because no a priori assumptions about the number of free temperature bins are made, while the total number of free parameters stays approximately the same and the contribution of a temperature bin to the spectrum is directly comparable between the quiescent and the active states. This fit results in proper uncertainties for EM values and abundances. The 10-temperature fits to the spectra of the quiescent state and the active state are shown in Fig. 2. The thick solid line is the model. The top panel corresponds to the quiescent state and the bottom panel to the active state. The values of the fit are collected in Table 2. This table shows the interstellar column density N_H, the fixed T-values (identical for the quiescent and active spectra), the EMs, the luminosities of the different temperature bins, the electron densities, and abundances. The latter are relative to solar photospheric values (Anders & Grevesse 1989), except for iron and oxygen. For Fe the values of (Grevesse & Sauval 1998, 1999) and for O the values by Allende Prieto & Lambert (2001) have been applied. The EM is defined as EM = $n_e n_H V$, in which $n_H = 0.85 n_e$. The X-ray luminosity is given over the energy range from 0.3 to 10 keV. For the luminosities no individual statistical errors have been determined. Their uncertainties are supposed to have the same relative values as those for the EMs because the luminosity is mostly determined by the EMs in this temperature range, and therefore $L_X \propto EM$. Also a flux normalization factor between RGS and the EPIC instruments is used. This normalization factor is between 1.1 and 1.2 for both instruments (pn and MOS). A slight shift in λ ($\approx$4.4e−4) was applied to optimize the wavelength calibration.

The abundances are similar for the quiescent and active parts. In both cases a depletion of elements with a low FIP (IFIP effect) can be noted (Table 2 and Fig. 3). This trend is similar to the one observed in AT Mic (Raassen et al. 2003a). However, there a slight suppression of this IFIP effect in the active state was seen, which is not present in the spectrum of YZ CMi.
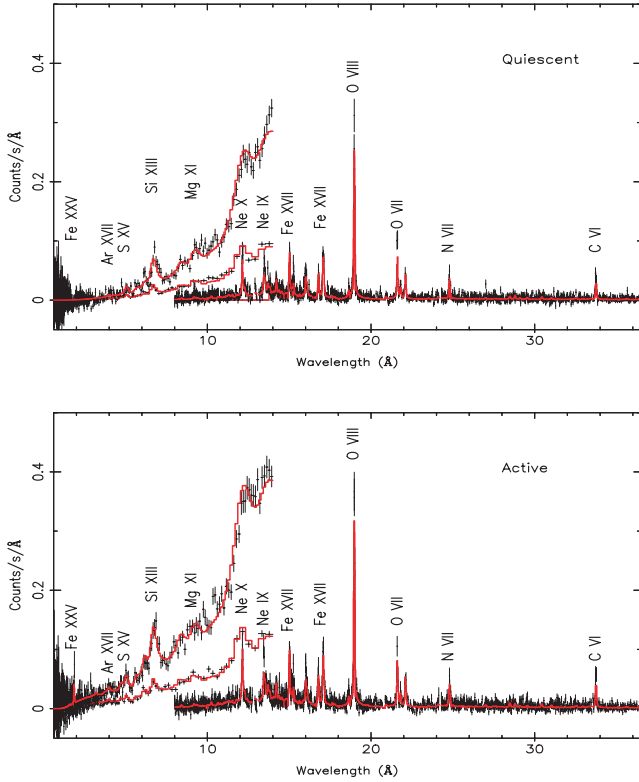
Figure 2. The fitted spectra of the quiescent state (top panel) and active state (bottom panel) of YZ CMi, applying a 10-temperature fit with fixed temperature bins (see Table 2). The solid line (red in the electronic version) is the fit.
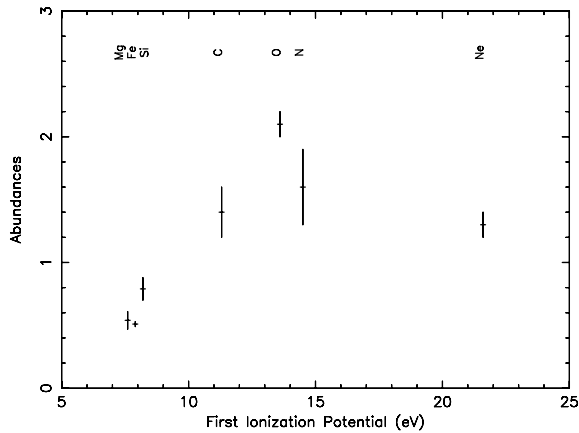

Figure 3. Abundances versus the FIP. Due to the similarity of the abundances in the quiescent and active states, only the values for the quiescent state are given. The following FIP values (eV) have been used: C = 11.3; N = 14.5; O = 13.6; Ne = 21.6; Mg = 7.6; Si = 8.2; and Fe = 7.9 (Kelly 1987).

3.2 A 10-temperature model for the individual flares

Apart from the quiescent and the active parts time-cuts have also been prepared for the individual flares. The time-intervals are 1.6 and 2.3 ks for flare 1 and 2, respectively. These intervals are too short to extract reliable spectra to fit statistically relevant abundances. Assuming a relatively small stellar surface to be flaring, however, it is possible to quantify the flare plasma by assuming that the non-flaring plasma is still described by the model we have

Table 2. Multi-temperature fit (see the text), obtained from a model with fixed temperatures from 0.02 to 10.24 keV with a log step size of 0.3 (i.e. a factor of 2). Elemental abundances are relative to the solar photospheric values of Anders & Grevesse (1989) (except for Fe and O). The X-ray luminosity is given over the energy range from 0.3 to 10 keV. In parentheses statistical 1σ errors are given.

Parameters	Quiescent	Active
$\log N_{\rm H}$ (cm^{-2})	18.08	18.08
EPIC-MOS/RGS		1.187
EPIC-pn/RGS		1.135
T_1 (keV)	0.02	
T_2 (keV)	0.04	
T_3 (keV)	0.08	
T_4 (keV)	0.16	
T_5 (keV)	0.32	
T_6 (keV)	0.64	
T_7 (keV)	1.28	
T_8 (keV)	2.56	
T_9 (keV)	5.12	
T_{10} (keV)	10.24	
EM$_{1-3}$	0.0	0.0
EM$_4$ (10^{50} cm^{-3})	1.5(.3)	1.7(.4)
EM$_5$ (10^{50} cm^{-3})	3.0(.5)	4.0(.6)
EM$_6$ (10^{50} cm^{-3})	8.4(.5)	10.9(.7)
EM$_7$ (10^{50} cm^{-3})	0.5(.3)	1.4(.7)
EM$_8$ (10^{50} cm^{-3})	0.3(.2)	3.7(.6)
EM$_{9-10}$	0	0
EM$_{\rm Tot}$ (10^{50} cm^{-3})	13.7(.8)	21.7(1.4)
$n_{\rm e}$O VII (10^{10} cm^{-3})	2.4(1.8)	$\lesssim$1.9
$n_{\rm e}$Ne IX (10^{12} cm^{-3})	$\lesssim$1.7	$\lesssim$4.2
$L_{\rm X1-3}$	0	0
$L_{\rm X4}$ (10^{27} erg s^{-1})	2.1(–)	2.4(–)
$L_{\rm X5}$ (10^{27} erg s^{-1})	5.0(–)	6.5(–)
$L_{\rm X6}$ (10^{27} erg s^{-1})	13.4(–)	17.4(–)
$L_{\rm X7}$ (10^{27} erg s^{-1})	0.7(–)	1.8(–)
$L_{\rm X8}$ (10^{27} erg s^{-1})	0.3(–)	5.2(–)
$L_{\rm X9-10}$	0	0
$L_{\rm Tot}$ (10^{27} erg s^{-1})	21.5(–)	33.3(–)
C	1.1(.2)	1.1(.2)
N	1.4(.3)	1.3(.3)
O	1.7(.1)	1.6(.1)
Ne	1.3(.1)	1.3(.1)
Mg	0.51(.08)	0.58(.09)
Si	0.76(.10)	0.91(.10)
Fe	0.40(.02)	0.40(.03)
χ^2/d.o.f.	1082/867	1100/868
$\chi^2_{\rm red}$	1.24	1.27

derived above, while the flare plasma is described by additional thermal components. For flare 1 only one additional temperature bin could be determined. For comparison a fit with one additional temperature was made for both flares. The derived temperatures are average temperatures of the flares. These values are collected in Table 3 (top). For flare 2, however, a wider spread temperature pattern could be established. To determine a maximum temperature for this flare, the additional three EMs and one of the additional temperatures (the highest one) were free to vary. The derived values are collected in Table 3 (bottom). For fitted parameters statistical 1σ errors are given in parentheses. The values are related to T_{6-8} in Table 2 of the multi-temperature fitting. This method shows the

Table 3. Temperature and EM fit to the individual flares by adding additional temperatures and EMs to the values obtained for the quiescent state (from Table 2). The latter were fixed during the fit procedure (see the text). The results of adding one temperature bin are shown at the top of the table, while the results of a multi-temperature fit to flare 2 are given at the bottom (see the text). For fitted parameters statistical 1σ errors are given in parentheses. The X-ray luminosity is given over the energy range from 0.3 to 10 keV.

Parameters	Flare 1	Flare 2
T_1 (keV)	1.19(.10)	1.22(.05)
EM_1 (10^{50} cm^{-3})	5.5(.5)	14.1(.5)
L_{X1} (10^{27} erg s^{-1})	7.1(.−)	18.3(.−)
χ^2_{red}	1.25	1.50
T_1 (keV)	–	0.64
EM_1 (10^{50} cm^{-3})	–	5.6(1.1)
L_{X1} (10^{27} erg s^{-1})	–	9.0(.−)
T_2 (keV)	–	1.28
EM_2 (10^{50} cm^{-3})	–	4.0(1.8)
L_{X2} (10^{27} erg s^{-1})	–	5.1(.−)
T_3 (keV)	–	2.9(.5)
EM_3 (10^{50} cm^{-3})	–	5.5(1.3)
L_{X3} (10^{27} erg s^{-1})	–	8.1(.−)
EM_{Total} (10^{50} cm^{-3})	–	15.1(2.4)
L_{Total} (10^{27} erg s^{-1})	–	22.2(.−)
χ^2_{red}	–	1.22

excess of emission caused by the flares. The calculations show that the additional component especially affects the hot plasma below 10 Å, but does not affect significantly the O VII and Ne IX line triplets.

3.3 Differential EM modelling

To show the smooth connection between the separated temperature bins, we have performed a differential EM modelling for the spectrum of YZ CMi in the quiescent state, the active state, and flare 2, applying the regularization method in the SPEX code. This method uses direct matrix inversion with the additional constraint that the second-order derivative of the solution with respect to the temperature is as smooth as possible (Kaastra et al. 1996b). In this differential EM modelling, the abundances given in Table 2 have been used. The results are shown in Fig. 4. The results of the fits, collected in Table 2, Table 3 and Fig. 4, are in good agreement with
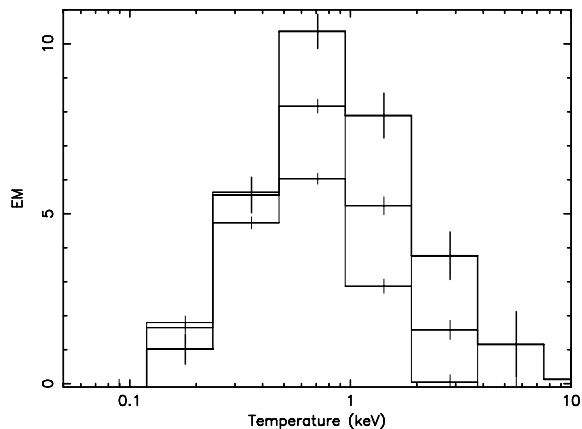

Figure 4. Differential EM modelling of YZ CMi, based on the regularization method (see the text). The thin line reflects the EM of the quiescent state. The thicker line corresponds to the active state and the bold line corresponds to flare 2. The EM is given in units of 10^{50} cm^{-3}.

Table 4. Line fluxes at the Earth of YZ CMi measured with EPIC-pn and RGS. Statistical 1σ errors are in parentheses.

Ion	λ_0^a (Å)	λ_{obs}^b (Å)	Flux^c	λ_{obs} (Å)	Flux
			Quiescent		Active
pn					
Fe XXV	1.855	1.855^d	$\lesssim$0.002	1.855^d	0.03(.01)
Ar XVII	3.96	3.96^d	$\lesssim$0.02	3.96^d	0.05(.02)
S XVI	4.73	4.73^d	0.03(.02)	4.73^d	0.04(.03)
S XV	5.066	5.066^d	0.04(.02)	5.066^d	0.13(.03)
Si XIV	6.183	6.183^d	0.05(.02)	6.183^d	0.08(.03)
Si XIII	6.688	6.792(.037)	0.17(.03)	6.764(.044)	0.27(.04)
RGS					
Ne X	12.134	12.142(.009)	1.4(.2)	12.144(.009)	1.8(.3)
Ne IX	13.447	13.463(.023)	0.9(.4)	13.452(.009)	1.7(.3)
Ne IX	13.553	13.526(.028)	0.6(.4)	13.591(.019)	0.8(.2)
Ne IX	13.700	13.697(.018)	0.5(.2)	13.722(.023)	0.5(.2)
Fe XVII	13.834	–	–	13.850(.023)	0.4(.2)
Fe XVIII	14.202	14.216(.028)	0.4(.2)	14.245(.018)	0.6(.2)
Fe XVII	15.013	15.029(.009)	1.0(.2)	15.021(.006)	1.5(.2)
O VIII	15.176	15.175(.051)	0.1(.1)	15.187(.042)	0.4(.4)
Fe XVII	15.260	15.259(.014)	0.5(.2)	15.256(.037)	0.6(.4)
O VIII	16.006	15.999(.014)	0.9(.2)	16.018(.007)	1.1(.2)
Fe XVII	16.775	16.791(.009)	0.8(.2)	16.780(.008)	1.0(.2)
Fe XVII	17.051	17.056(.019)	0.9(.4)	17.051^d	0.8(.3)
Fe XVII	17.100	17.110(.018)	1.0(.4)	17.100^d	1.1(.3)
O VII	18.627	18.666(.148)	0.2(.2)	18.619(.016)	0.5(.1)
O VIII	18.969	18.978(.006)	4.9(.5)	18.976(.004)	6.0(.5)
O VII	21.602	21.602(.005)	2.2(.3)	21.600(.009)	2.2(.4)
O VII	21.804	21.799(.018)	0.6(.2)	21.822(.018)	0.5(.2)
O VII	22.101	22.105(.009)	1.1(.2)	22.106(.018)	1.4(.3)
N VII	24.781	24.795(.014)	0.9(.2)	24.800(.014)	0.7(.2)
C VI	33.736	33.741(.014)	1.7(.3)	33.740(.005)	2.0(.3)

$^a\lambda_0$ are the theoretical energy and wavelength from Kelly (1987).
$^b\lambda_{obs}$ is the observed wavelength with the statistical 1σ error in parentheses.
^{c}In units of 10^{-4} photons cm^{-2} s^{-1}.
^{d}Fixed to the theoretical value.

each other. We note higher EM values for the active state and for flare 2 in the temperature range from 0.6 to 3 keV, while those of the other temperatures are similar for the three states.

4 INDIVIDUAL LINE FLUXES

The individual line fluxes of the spectra of the quiescent state and the active state have been measured. We use RGS data where available, and EPIC-pn at short wavelengths. For each observed line a Gaussian profile was folded through the response matrix and fitted to the observed line profile, establishing the positions, fluxes as well as the widths of the lines. Apart from the instrumental broadening, no additional line broadening was noted. The measured wavelengths and line fluxes are collected in Table 4 together with the theoretical wavelengths from laboratory measurements (Kelly 1987). Some minor wavelength deviations of a few mÅ towards higher wavelengths seem to be present. This is comparable with the instrumental wavelength accuracy. No systematic line shifts between the two states (quiescent and active) are found.

The line fluxes of the higher ionized ions, such as O VIII, Ne IX–X, Si XIII–XIV, S XV–XVI, Ar XVII and Fe XXV, are slightly higher in the active state than in the quiescent state, reflecting the larger EM at

higher temperatures. However, the uncertainties in the measured line fluxes are relatively large compared to these differences.

5 DENSITY DETERMINATION

By definition, the determination of the EM in combination with the determination of the electron density n_e offers the possibility to derive the emitting volume, assuming a source with spatially constant n_e. The individual line fluxes of the line triplets in the He-like ions, consisting of a resonance line (r), an intercombination line (i) and a forbidden line (f), are strong tools for density diagnostics (Gabriel & Jordan 1969). The ratios of the fluxes of the forbidden line to the intercombination line (f/i) of C V, N VI, O VII, Ne IX, Mg XI and Si XIII serve as density diagnostic for the spectra in the wavelength range from 5 to 45 Å which lies in the sensitivity range of *Chandra* and *XMM–Newton*. Here, we focus on the ions O VII and Ne IX. The He-like carbon lines are outside the wavelength range of RGS and the nitrogen lines are too weak, while those of magnesium and silicon are weak and not well separated. We determine the densities in two ways: once via the multi-temperature fitting and then by measuring individual line fluxes.

After the final overall multi-temperature fit, two limited wavelength ranges (21.4–22.4 Å for O VII and 13.2–14 Å for Ne IX) were selected to determine the density based on the He-like line triplets of oxygen and neon. During this fit all parameters of the above models were fixed, except the density and the related abundance (oxygen when fitting the range 21.4–22.4 Å and neon when fitting the range 13.2–14 Å). The abundances served as normalization parameters. The advantage of fitting the density as part of the multi-temperature fit is that all blends (and very weak lines that contribute to a pseudo-continuum) are taken into account with the correct flux as obtained from the multi-temperature model. The electron densities obtained from the O VII line triplet are $n_e = 2.4(1.8) \times 10^{10}$ and $n_e \lesssim 1.9 \times 10^{10}$ cm^{-3}, for the quiescent and active states, respectively. The densities based on Ne IX are $n_e \lesssim 1.7 \times 10^{12}$ cm^{-3} for the quiescent state and $n_e \lesssim 4.2 \times 10^{12}$ cm^{-3} for the active state. The O VII lines in the active state and the Ne IX lines only yield upper limits.

Considering the measured line fluxes (see Table 4), the f/i ratios of O VII and Ne IX in the quiescent state are 1.91(.68) and 1.04(.88), respectively. In the active state the f/i ratios are 2.84(1.40) for O VII and 0.57(.26) for Ne IX. Within the error bars the values for O VII are equal. As O VII will be ionized above $T \gtrsim 5$ MK, both values reflect the quiescent plasma. This is supported by the fact that EM$_4$ and EM$_5$ (see Table 2), which are responsible for O VII, remain the same during the flare. Based on the most accurate value of f/i = 1.91(.68) a value for $n_e = 3.5(-1.9, +3.8) \times 10^{10}$ cm^{-3} is determined (Porquet et al. 2001). This is in agreement with the values obtained from the multi-temperature fit (see Table 2). Our best values for the quiescent state [$n_e = 2.4(1.8) \times 10^{10}$ cm^{-3} and $n_e = 3.5(-1.9, +3.8) \times 10^{10}$ cm^{-3}] are in very good agreement with the values by Ness et al. (2004) derived from the total spectrum. They give $n_e = 3.2(-0.9, +1.3) \times 10^{10}$ cm^{-3}. Thanks to the better S/N as a result of the use of the total observation, their errors are smaller. Although based on the total spectrum (including quiescent and active areas), their n_e value reflects the density of the quiescent plasma, as explained above. This n_e value is applied as the pre-flare density n_0 in the formulae of the next section.

For Ne IX the uncertainties are large and the wavelengths of the lines deviate considerably from the theoretical wavelengths (Kelly 1987). The latter is an indication for the presence of the known Fe blends in the Ne IX line-triplet. Therefore, the densities derived from the Ne IX lines at RGS resolution are not reliable.

6 LOOP LENGTHS AND MAGNETIC FIELD STRENGTHS

In addition to the spectral information, the flare light curves contain valuable information about periodicity, rise and decay times, as well as the ratio between maximum and minimum count rates, which can be used to determine the spatial dimension of the flare. Additionally, scaling laws also provide estimates on the flare loop length as well as the local magnetic field strength.

In a recent paper, Mitra-Kraev et al. (2005b) apply three different methods to determine the characteristic length of the magnetic flare structure (L) and the magnetic field strength (B) of a stellar flare, namely magneto-acoustic waves (Roberts, Edwin & Benz 1984; Zaıtsev & Stepanov 1989), PB scaling laws (Shibata & Yokoyama 1999, 2002), and radiative cooling (Hawley et al. 1995). In the absence of a clear wave signature, only the last two methods are applied to the flares of YZ CMi, the results of which are presented in this section.

We use the spectral results from the previous sections, namely the single flare temperatures and EMs from Table 3, and the quiescent pre-flare electron density determined by Ness et al. (2004) from the O VII f/i line ratio, as discussed in Section 5. The average temperature and EM values determined in Section 3 for flare 2 by the other methods are all in agreement with the single temperature fit, while flare 1 only has one temperature.

The PB scaling laws derived by Shibata & Yokoyama (2002) give expressions for the flare's magnetic field strength B and characteristic length of the loop L in dependence of EM, the pre-flare electron density n_0 and flare temperature T:

$$B(\mathrm{PB}) = 50 \left(\frac{\mathrm{EM}}{10^{48} \ \mathrm{cm}^{-3}} \right)^{-1/5} \left(\frac{n_0}{10^9 \ \mathrm{cm}^{-3}} \right)^{3/10} \left(\frac{T}{10^7 \ \mathrm{K}} \right)^{17/10} \mathrm{G},$$

$$L(\mathrm{PB}) = 10^9 \left(\frac{\mathrm{EM}}{10^{48} \ \mathrm{cm}^{-3}} \right)^{3/5} \left(\frac{n_0}{10^9 \ \mathrm{cm}^{-3}} \right)^{-2/5} \left(\frac{T}{10^7 \ \mathrm{K}} \right)^{-8/5} \mathrm{cm}.$$

In their derivations, they use simple order-of-magnitude estimates, for example, the emitting volume is given by $V = L^3$. However, from *TRACE* observations we know that very large flares usually appear as arcades, containing many narrow individual loops. Another geometry of the flare than the one chosen by Shibata & Yokoyama (2002) will influence our obtained loop length. Since the shapes of the flares will be different from flare to flare and from stellar source to stellar source, we have applied the commonly used shape, given by Shibata & Yokoyama.

From numerical simulations, Shibata & Yokoyama (2002) estimated that the flare temperature T is about a factor of 3 lower than the flare's maximal temperature $T_{\max}$. This is in agreement with the observation of flare 2 of YZ CMi, where the one-temperature-fit temperature is $T = 1.22$ keV and the upper limit of the highest contributing temperature is $T_{\max} = 3.4$ keV for bin (T_3) in Table 3 and $T_{\max} = 3.8$ keV in Fig 4. For flare 1, however, our results yield only one average temperature component $T = 1.19$ keV.

Hawley et al. (1995) derive an expression for the loop length from the temporal shape of a flare, using flare heating and cooling rates (RC). They assume ionization equilibrium. On time-scales, as seen in these flares, ionization equilibrium should be attained especially for the heavier elements (Fe, S, Si, Mg). The influence of departure from ionization equilibrium is calculated to be less than 9 per cent (Spadaro et al. 1990).
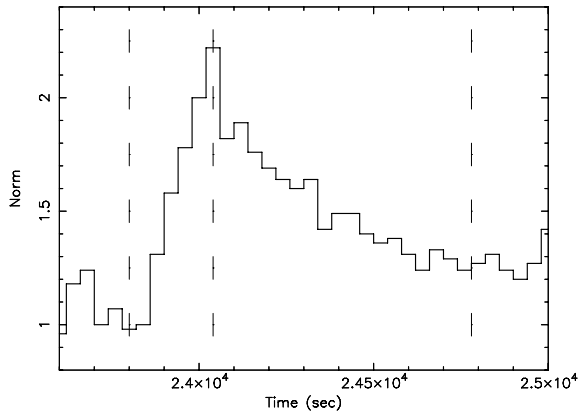
Figure 5. Flare 2 in the spectrum of YZ CMi, observed with EPIC-mos. The time-resolution of the curve is binned to 40 s. The start of rise, top, and end of decay of the flare are indicated.

Here, we use their expression in the form (see Mitra-Kraev et al. 2005b):

$$L(\mathrm{RC}) = \frac{1500}{\left(1 - x_{\mathrm{d}}^{1.58}\right)^{4/7}} \, \tau_{\mathrm{r}}^{3/7} \, \tau_{\mathrm{d}}^{4/7} \, (T_{\max})^{1/2},$$

where $T_{\max}$ is the maximal flare temperature, τ_{r} and τ_{d} rise and decay times of the flare, and x_{d} is the square root of the ratio between the count rate after flare decay and maximum count rate. Since no maximum temperature was established for flare 1, this method was applied to flare 2 only. Fig. 5 displays the blown-up light curve of flare 2, indicating the start, peak and end time of the flare. The figure shows the summed light curves obtained with EPIC-pn and EPIC-MOS, scaled so that the quiescent value equals 1.

Table 5 summarizes the obtained magnetic field strength (B) and characteristic lengths of the magnetic flare structures (L) derived from the two different models for both flares, as well as the input values. The obtained magnetic field strengths between 50 and 100 G and loop lengths of $\approx 10^{10}$ cm agree well with solar and other stellar flare values.

7 DISCUSSION AND CONCLUSIONS

We have studied the temporal X-ray behaviour of the nearby active M dwarf, YZ CMi. The star shows both quiescent and flaring periods for which we have extracted high-quality spectra from the RGS and EPIC instruments. We have in particular studied differences

Table 5. Derived magnetic field strengths and characteristic lengths of the magnetic flare structures

Parameter	Flare 1	Flare 2
T (keV)	1.2(.1)	1.22(.05)
T (MK)	14(1)	14.2(.6)
$T_{\max}$ (MK)	–	42(2)
EM (10^{50} cm^{-3})	5.5(.5)	14.1(.5)
n_0(10^{10} cm^{-3})	3(1)	3(1)
x_{d}	–	0.77(.04)
τ_{r} (s)	–	240(40)
τ_{d} (s)	–	740(150)
B(PB) (G)	70(20)	60(10)
L(PB)(10^9 cm)	7(2)	11(2)
L(RC)(10^9 cm)	–	8(2)

between the two states in terms of thermal structure and composition. Although the active episode clearly shows enhanced EM at high temperatures as would be expected for flares, no difference in the elemental composition could be identified. We thus see no evidence for a change in the element fractionation during the flares. However, we need to caution that many spectral lines, in particular those formed at low temperatures, are originating from the non-flaring plasma as their flux did not change between the two activity states.

Using spectral and light curve properties of the flares, we estimated the coronal magnetic field strengths between 50 and 100 G and flare loop lengths of $\approx 10^{10}$ cm. This is comparable to the values obtained by Mitra-Kraev et al. (2005b) for AT Mic applying the same methods and with values given in a study by Mullan et al. (2006). Our loop length is somewhat larger than the values obtained by Welsh et al. (2006) for other flaring dMe-type stars. Their value was based on oscillations observed in the ultraviolet, probably originating from different structures.

As discussed before any difference in geometry of the flare will influence the values, when applying the method outlined by Shibata & Yokoyama (1999, 2002). Ionization equilibrium, as assumed in the method of Hawley et al. (1995), should be attained on time-scales as seen in these flares, especially for the heavier elements (Fe, S, Si, Mg). Departure from ionization equilibrium for the lighter elements (C and O) will influence the loop length by less than 9 per cent (Spadaro et al. 1990). This uncertainty is far less than uncertainties in the loop length due to uncertainties in our measured values of EM, T and n_{e}.

The flare loop length is about 40 per cent of YZ CMi's radius ($R_{\mathrm{YZCMi}} \approx 2.6 \times 10^{10}$ cm). Such relatively large loops are often inferred in active M dwarfs (Pettersen 1980). These stars distinguish themselves by being very X-ray active. Their X-ray-to-bolometric luminosity ratio is of the order of 10^{-3}, compared to 10^{-6} for the active and 10^{-7} for the quiet Sun. These stars have comparable or even stronger magnetic fields than the Sun, which may be due to the convective zone reaching far into the star's interior. These magnetic fields support high coronal activity as witnessed by their strong X-ray emission and frequent flare occurrence rate. The observed magnetic field strength of 50 to 100 G is at the upper end of the supposed magnetic field strengths possible in stellar coronae. It seems that the large loops are a direct manifestation of these strong fields.

The values we derived are somewhat smaller than the extent of the radio corona above the photosphere of $\approx 1.77 \times 10^{10}$ cm (Pestalozzi et al. 2000). Although closed magnetic fields thus appear to reach out to larger distances from the stellar surface (as evidenced by radio observations), the high-density regions that appear bright in X-rays are relatively compact. This is not different from the solar corona.

Despite the considerable difference between the activity level of this star and the Sun as well as its much lower mass, we suggest that X-ray activity is determined by active regions that overall are similar to those found on the Sun. This further supports the finding by Güdel et al. (2004) and Reale et al. (2004) who modelled flaring active regions on Proxima Centauri, a star with a similar activity level to YZ CMi.

ACKNOWLEDGMENTS

REFERENCES

Allende Prieto C., Lambert D. L., 2001, ApJ, 556, L63

Anders E., Grevesse N., 1989, Geochim. Cosmochim. Acta, 53, 197

Arnaud M., Rothenflug R., 1985, A&AS, 60, 425

Audard M., Güdel M. R., Mewe R., 2001, A&A, 365, L318

Audard M., Güdel M., Sres A., Raassen A. J. J., Mewe R., 2003, A&A, 398, 1137

Audard M., Telleschi A., Güdel M., Skinner S. L., Pallavicini R., Mitra-Kraev U., 2004, ApJ, 617, 531

Brinkman A. C. et al., 2000, ApJ, 530, L111

Brinkman A. C. et al., 2001, A&A, 365, L324

Canizares C. R. et al., 2000, ApJ, 539, L41

Doschek G. A., Feldman U., Landecker P. B., McKenzie D. L., 1981, ApJ, 249, 372

Feldman U., 1992, Phys. Scr., 46, 202

Gabriel A. H., Jordan C., 1969, MNRAS, 145, 241

Grevesse N., Sauval A. J., 1998, Space Sci. Rev., 85, 161

Grevesse N., Sauval A. J., 1999, A&A, 347, 348

Güdel M., 2004, A&AR, 12, 71

Güdel M., Audard M., Skinner S. L., Horvath M. I., 2002, ApJ, 580, L73

Güdel M., Audard M., Reale F., Skinner S. L., Linsky J. L., 2004, A&A, 416, 713

Güdel M., Linsky J. L., Brown A., Nagase F., 1999, ApJ, 511, 405

Hawley S. L. et al., 1995, ApJ, 453, 464

Jansen F. et al., 2001, A&A, 365, L1

Jordan C., Doschek G. A., Drake J. J., Galvin A. B., Raymond J. C., 1998, in Donahue R. A., Bookbinder J. A., eds, ASP Conf. Ser. Vol., 10th Cambridge Workshop on Cool Stars, Stellar Systems, and the Sun. Astron. Soc. Pac., San Francisco, p. 91

Kaastra J. S., Mewe R., Nieuwenhuijzen H., 1996a, in Yamashita K., Watanabe T., eds, UV and X-ray Spectroscopy of Astrophysical and Laboratory Plasmas. Universal Academy Press, Inc., Tokyo, p. 411 (SPEX)

Kaastra J. S., Mewe R., Liedahl D. A., Singh K. P., White N. E., Drake S. A., 1996b, A&A, 314, 547

Kelly R. L., 1987, J. Phys. Chem. Rev. Data, 16, Suppl. 1

Laming J. M., 2004, ApJ, 614, 1063

Lim J., Vaughan A. E., Nelson G. J., 1987, Proc. Astron. Soc. Aust., 7, 197

Mewe R., Kaastra J. S., Liedahl D. A., 1995, Legacy, 6, 16 (MEKAL)

Mewe R., Kaastra J. S., van den Oord G. H. J., Vink J., Tawara Y., 1997, A&A, 320, 147

Mitra-Kraev U. et al., 2005a, A&A,, 431, 679

Mitra-Kraev U., Harra L. K., Williams D. R., Kraev E., 2005b, A&A, 436, 1041

Mullan D. J., Doyle J. G., Redman R. O., Mathioudakis M., 1992, ApJ, 397, 225

Mullan D. J., Mathioudakis M., Bloomfield D. S., Chriastian D. J., 2006, ApJS, 161, 173

Ness J.-U., Güdel M., Schmitt J. H. M. M., Audard M., Telleschi A., 2004, A&A, 427, 667

Osten R. A., Brown A., Ayres T. R., Linsky J. L., Drake S. A., Gagné M., Stern R. A., 2000, ApJ, 544, 953

Osten R. A., Ayres T. R., Brown A., Linsky J. L., Krishnamurthi A., 2003, ApJ, 582, 1073

Perryman M. A. C. et al., 1997, A&A, 323, L49

Pestalozzi M. R., Benz A. O., Conway J. E., Güdel M., 2000, A&A, 353, 569

Pettersen B. R., 1980, A&A, 82, 53

Pettersen B. R., 1989, Sol. Phys., 121, 299

Porquet D., Mewe R., Dubau J., Raassen A. J. J., Kaastra J. S., 2001, A&A, 376, 1113

Raassen A. J. J., 2005, in Favata F., Hussain G. A. J., Battrick B., eds, ESA SP-560, Proc. 13th Cambridge Workshop on Cool Stars, Stellar Systems and the Sun. ESA, Noordwijk, p. 887

Raassen A. J. J., Mewe R., Audard M., Güdel M., 2003a, A&A, 411, 509

Raassen A. J. J., Ness J.-U., Mewe R., van der Meer R. L. J., Burwitz V., Kaastra J. S., 2003b, A&A, 400, 671

Reale F., Güdel M., Peres G., Audard M., 2004, A&A, 416, 733

Roberts B., Edwin P. M., Benz A. O., 1984, ApJ, 279, 857

Shibata K., Yokoyama T., 1999, ApJ, 526, L49

Shibata K., Yokoyama T., 2002, ApJ, 577, 422

Smith K. W., Güdel M., Audard M., 2005, A&A, 436, 241

Spadaro D., Zappalà R. A., Antiochos S. K., Lanzafame G., Noci G., 1990, ApJ, 362, 370

Telleschi A., Güdel M., Briggs K., Audard M., Ness J.-U., Skinner S. L., 2005, ApJ, 622, 653

Welsh B. Y. et al., 2006, A&A, 458, 921

White N. E. et al., 1994, PASJ, 46, L97

Zaıtsev V. V., Stepanov A. V., 1989, Sov. Astron. Lett., 15, 66

This paper has been typeset from a TEX/LATEX file prepared by the author.